SUPPLEMENTAL MATERIAL for

Near-Field Fluorescence Cross-Correlation Spectroscopy On Planar Membranes

Christopher V. Kelly,[a, b, c, *] *Devin L. Wakefield,*[a] *David A. Holowka,*[a] *Harold G. Craighead,* [b] *and Barbara A. Baird* [a]

[a] Department of Chemistry and Chemical Biology, Cornell University, Ithaca, New York 14853

[b] School of Applied and Engineering Physics, Cornell University, Ithaca, New York 14853

[c] Department of Physics and Astronomy, Wayne State University, Detroit, MI 48201

SUPPLEMENTAL TEXT

Varying Aperture Properties in Finite Element Analysis Simulations

Computational analysis of the illumination profile provides a relatively inexpensive and rapid means of testing the experimental variables that may influence the illumination profile vs. experimentally measuring the illumination profile. Three-dimensional finite element analysis (FEA) simulations were performed in the electromagnetic module of COMSOL Multiphysics (COMSOL, Inc.) with a perfectly matched boundary layer condition.[1,2] All simulation results presented in the Supplemental Material are presented as an average over the azimuthal angle, yielding cylindrical symmetry, equivalent to circularly polarized or unpolarized incident light used in the experimental methods. The detailed material properties used for FEA simulations are tabulated in Table S1.

FEA was performed to simulate the light transmitted through an idealized, perfectly flat aperture with varying the aperture diameter, the index of refraction of the dielectric material filling the aperture, the index of refraction of the dielectric material coating the aperture, or the type of metal that is surrounding the aperture (Fig. S1). Smaller apertures yielded a more rapid decay of the transmitted light intensity both vertically and laterally away from the aperture center in addition to a weaker intensity of this transmitted light (Fig. S1A).

By filling and coating an aperture with a dielectric material of higher index of refraction, the wavelength light became smaller relative to the aperture diameter. The wavelength of the incident light was adjusted with the index of refraction of the aperture-filling and aperture-coating material, and the resulting illumination profile was not affected by the dielectric (Fig. S1B). The exception to this occurs when the filling and coating material is not fully transparent but rather has some absorption of the light, as represented by a complex index of reflection. When the material filling and coating the aperture slightly absorbs the light, the resulting transmitted illumination profile becomes smaller (Fig. S1B).

The material that fills the aperture affects the intensity of light transmitted through the aperture, but it does not affect the resulting illumination profile in the space above the aperture (Fig. S1C). Within these simulations, the 100 nm diameter apertures were coated with water (n = 1.33) and exposed to light with a free-space wavelength of 488 nm while the dielectric material filling the aperture was varied. Both the vertical and lateral illumination profiles overlap well for varying aperture-filling materials. However, a larger refractive index resulted in greater

transmission through the aperture. The in-material wavelength was smaller and the aperture attenuated the incident light less. Although the amount of transmitted light varied with the aperture-filling material, the material filling the aperture did not affect the illumination profile emanating from the aperture. This computational prediction was confirmed by experimental comparison of apertures with varying filling materials; the solidified photoresist pillars above apertures showed no experimental dependence on whether or not the apertures were initially filled with glass, allowing or disallowing the photoresist to penetrate into the apertures.

Varying the type of metal forming the aperture also affected the illumination profile (Fig. S1D). Aluminum and chrome films produced very similar illumination profiles. Aluminum has slightly more light transmission through the aperture than chrome, but the light profiles emanating from the chrome vs. aluminum apertures were otherwise indistinguishable. However, gold had a much greater light transmission in general and yielded an illumination profile that is less confined to the small volume directly above the aperture. This was likely due to the increased transmission of 488 nm light into gold vs. chrome or aluminum.

Fabrication

The fabrication of apertures includes the fabrication of pillars in the fused silica substrate (Fig. S2, S3) followed by the deposition of either an evaporated (Fig. S4) or a sputtered (Fig. S5) metal film and chemical mechanical polishing. These images demonstrate the size of the apertures and reveal the shape of the fused silica pillars between the surface of the apertures and the fused silica wafer.

Optical Alignment

Alignment of the optical components required careful, daily attention. Firstly, it was necessary to make the centers of the two objectives collinear and focused on the aperture. The bottom microscope objective was held in an inverted Olympus Inc. IX71 with its only degree of movement vertical to adjust the focal plane. The top microscope objective was held in an "Up-Down" microscope, sold in limited supply by Olympus Inc.. The Up-Down microscope consisted of an upright BX51 microscope body on an stand specifically designed to replace the top illuminator of the IX71. In addition to the control of the focal plane of the top objective with the focus knob on the Up-Down, the top microscope objective was held in a highly adjustable turret

that allowed for the lateral translation of the top objective relative to the microscope bodies (Olympus Inc.). Confirmation of this alignment was achieved by the presence of a semi-transparent sample that was well centered in the field of view of each objective with their respective eye-pieces.

Secondly, the illumination lasers were directed into a side-port of the fluorescent cube turret in the IX71 and directed up into the bottom of the bottom microscope objective by a 90% mirror. These lasers did not go through a tube lens before the bottom objective, so they came to a focused point in the center of the focal plane of the bottom objective. The lasers were well aligned when it entered the center of the bottom objective collinear to the objective center. This could be verified by observing the laser in the center of an alignment disk that was temporarily exchanged with the bottom microscope objective (Thorlabs Inc., VRC2RMS) and the laser traveling directly upward out of the center of the Up-Down's eye-pieces. (Caution: This method potentially exposes a focused laser into the user's eyes. Very low laser powers and extreme caution ought to be used.)

Thirdly, an array of apertures were held in the shared focal plane of the two objectives and a single aperture was centered with the focused laser spot. The aperture array was positioned with a piezoelectric nano-positioning stage (Mad City Labs Inc., LP-200). The aperture was well centered when the maximum light was transmitting through it, as detected through the eye-pieces, camera, or single photon counting module avalanche photodiodes (APD, PerkinElmer, SPCM-AQR-14-FC) on the Up-Down microscope.

Fourthly, the fluorescence emission collection optics were aligned. The fluorescence emission was focused by the top objective directly on to a optical fiber cable (OZ Optics, Ltd., QMMJ-33-UVVIS-100/140-3A-1) by a 4x microscope objective (Olympus Corp., PlanN). This system was attached to the back of the Up-Down microscope body, between the filter cube turret and the eye piece. Light was directed towards collection optics and away from the top eye-piece by a sliding 100% mirror (Olympus Corp.). The collection optics were held in place with 30 mm cube accessories (Thorlabs Inc.) and alignment was performed with translation stages (Thorlabs Inc., ST1XY-A and SM1Z) from a dichroic mirror (Semrock Inc., FF660-Di02-25x36) mounted within a cage cube (Thorlabs Inc., C6W and BC4). Emission channels were individually chromatically filtered (Semrock Inc., FF01-512/25 or Chroma Technology Corp., ET655lp) directly before being focused on to the optical fiber cable.

Finally, all optical components were aligned by maximizing the intensity of fluorescence emission collected by the APDs. The 30 mm cube translation stages holding the fiber optics needed the most attention. Control samples of densely labeled supported lipid bilayers were commonly used to achieve a constant bright fluorescence emission for alignment.

Measurement of D for CTxB

The diffusion rate of monomeric CTxB was measured with fluorescence recovery after photobleaching (FRAP) and single particle tracking (SPT) via stochastic optical reconstruction microscopy (STORM) (Fig. S6). The supported lipid bilayer of POPC with 0.1% GM1 was created on glass-bottom MatTek dish, as described in the Materials and Methods. CTxB-AF647 was bound to the membrane and its diffusion was monitored. Membrane formation, CTxB binding, and FRAP experiments were performed in a TRIS buffered saline (TBS, 50 mM TRIS, 150 mM NaCl, pH 8.5)

FRAP was performed with a Gaussian laser beam (w=9.1 μm) via traditional FRAP methods.[3] The optical setup included an Olympus IX83 microscope with a 100x objective (NA=1.49), a 2.5x magnifier, and an Andor iXon-Ultra camera acquiring an image every second. The images were then analyzed to plot the image intensity vs. time after a brief 1000x increase in the laser power to bleach all of the fluorophores within the laser spot. The K value of the bleaching was determined to be 12 by fitting the first images after bleaching. The recovery had a half time of 330 ± 20 sec and yielded D = 0.11 ± 0.02 sec.

SPT via STORM was performed similarly to sptPALM [4] and as described previously.[5] CTxB-AF647 was bound to the POPC and GM1 supported lipid bilayer on a glass-bottom MatTek dish. STORM imaging was performed on the same IX83 microscope described previously. The buffer during STORM imaging was specifically designed to enhance fluorophore blinking (50 mM TRIS, 150 mM NaCl, 133 mg/mL glucose, 40 μg/mL glucose oxidase, 3 μg/mL catalase, 10 μL/mL β-mercaptoethanol). 120 mW of 649 nm laser light was used to cause the majority of the AF647 within the laser spot to transition into a dark state with <2 fluorophores 'on' per 10 ms exposure for isolated determination of each fluorophore's location in each frame. The fluorophore locations were determined with PALM3D [6] and the tracks between sequential frames were determined via Track.m.[7] After localization and tracking of individual fluorophores, the mean square displacement (MSD) of each fluorophore was

determined as a function of the step time between frames (Δt). The slope of the MSD vs. Δt reveals the diffusion coefficient, which we determined to be 0.14 ± 0.1 $\mu m^2/s$.

The agreement from this FRAP and SPT result yields high confidence in our measurements. We average them to conclude that D for CTxB in a POPC supported lipid membrane to be 0.12 ± 0.03 $\mu m^2/s$.

SUPPLEMENTAL FIGURES

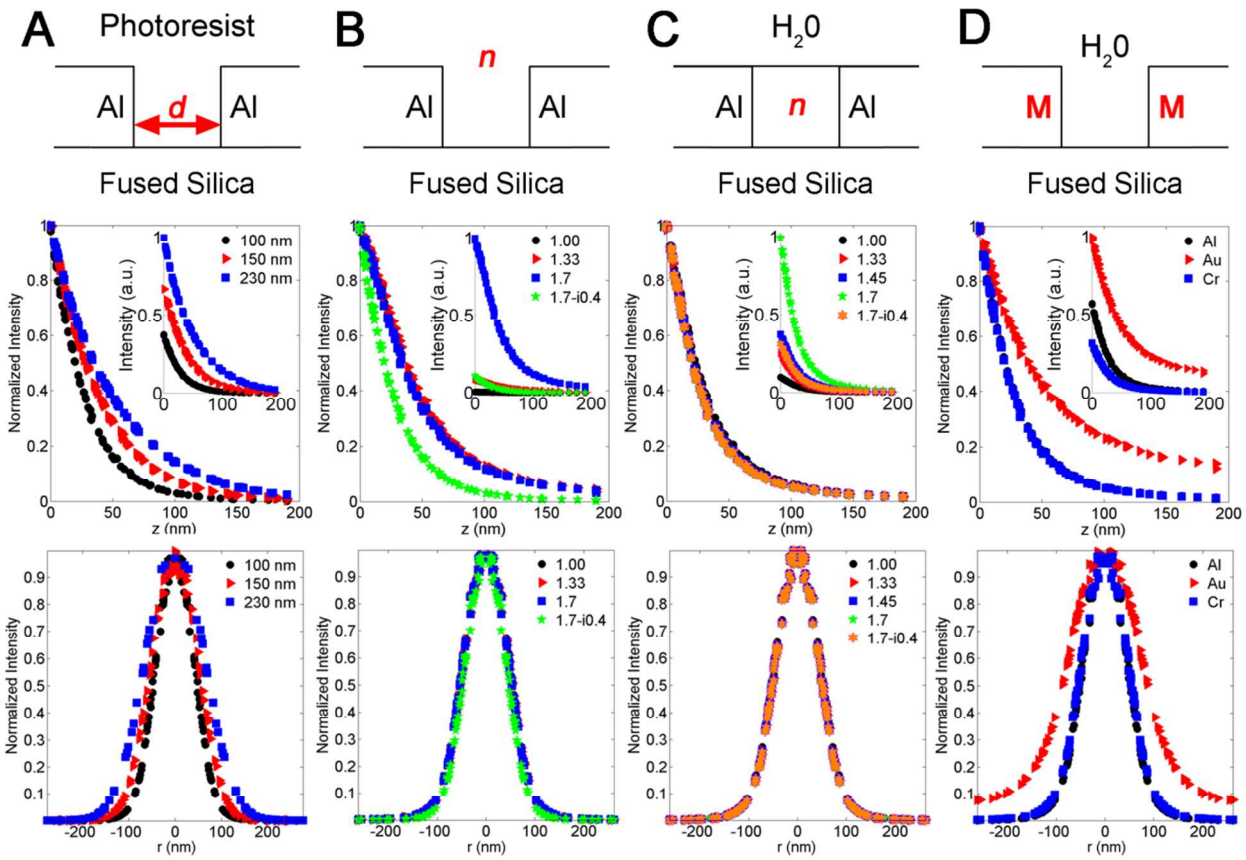

FIGURE S1: The properties of the illumination above idealized apertures were analyzed upon varying (A) the aperture diameter, (B) the material covering the aperture, (C) the material filling the aperture, and (D) the type of metal forming the aperture. In (A, C, D), light with a free-space wavelength of 488 nm was simulated. In (B), light with a free-space wavelength of 215, 279, and 365 nm were simulated for n = 1.00, 1.33, and 1.7, respectively to maintain a constant in-material wavelength. The normalized intensity vs. vertical distance (I vs. z) from the top of the aperture at r = 0 is shown in the middle row and unnormalized I vs. z is shown in the inset. The intensity vs. lateral position over the aperture (I vs. r) at z = 25 nm is shown in the bottom row. At z = 25, the contribution from the aperture rim as the rim-effect is strongly z-dependent, as shown in Fig. 2.

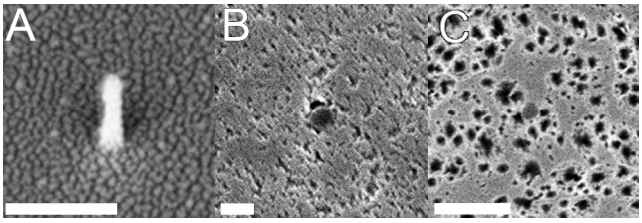

FIGURE S2: Scanning electron microscopy was used to inspect the apertures at the intermediate and final stages of fabrication. (A) Pillars of fused silica in before metal deposition are viewed at 45˚ from normal to observe their diameter (40 nm) and change in diameter with height. (B) Evaporation of Al and CMP provided planarized apertures that are clearly visible surrounded by the metal film. (C) Sputtering of Al-alloy provided a more conformal coating and fewer pinholes in the final 100 nm film than evaporated films, even though the glass-filled apertures were more difficult to observe via SEM due to the distinct metal grains. The scale bar in each frame represents 200 nm. More pillars and apertures such as these are shown in the Figs. S3-S5.

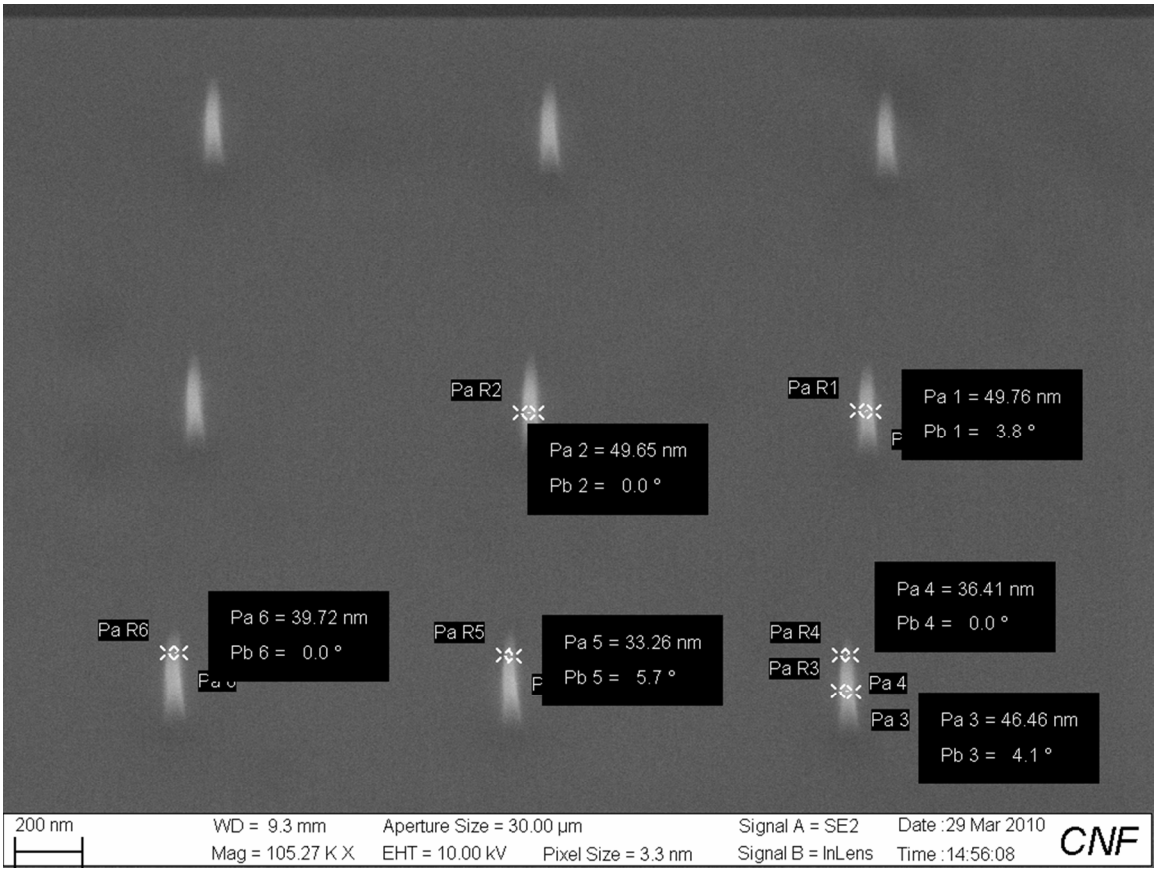

FIGURE S3: This SEM image of a fused silica wafer viewed from 45˚ from normal shows fused silica pillars created by electron-beam lithography and etching. These pillars represent an intermediate stage in aperture fabrication as they have yet to be coated with a thin, opaque metal film. These cylindrical pillars are 42 ± 7 nm diameter without significant tapering until their very top, which is sheared off during chemical mechanical polishing to leave only the bottom 100 nm on the wafer.

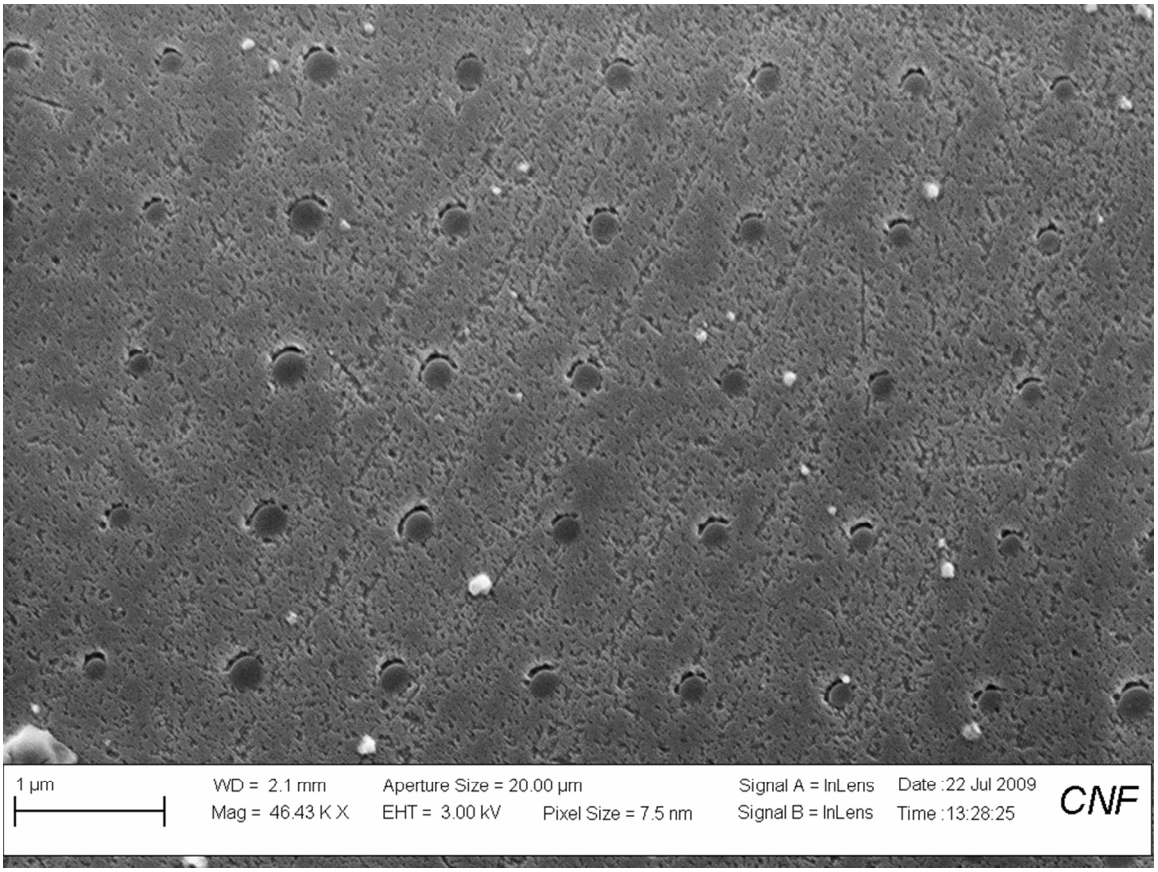

FIGURE S4: This SEM image of planarized aperture after the deposition of an aluminum thin film via evaporation shows variation in aperture size (140-240 nm diameter) and does not show the metal-alloy grains found in sputtered films. These apertures worked well for near-field fluorescence correlation spectroscopy, however there were occasional pinholes in the aluminum film to be avoided.

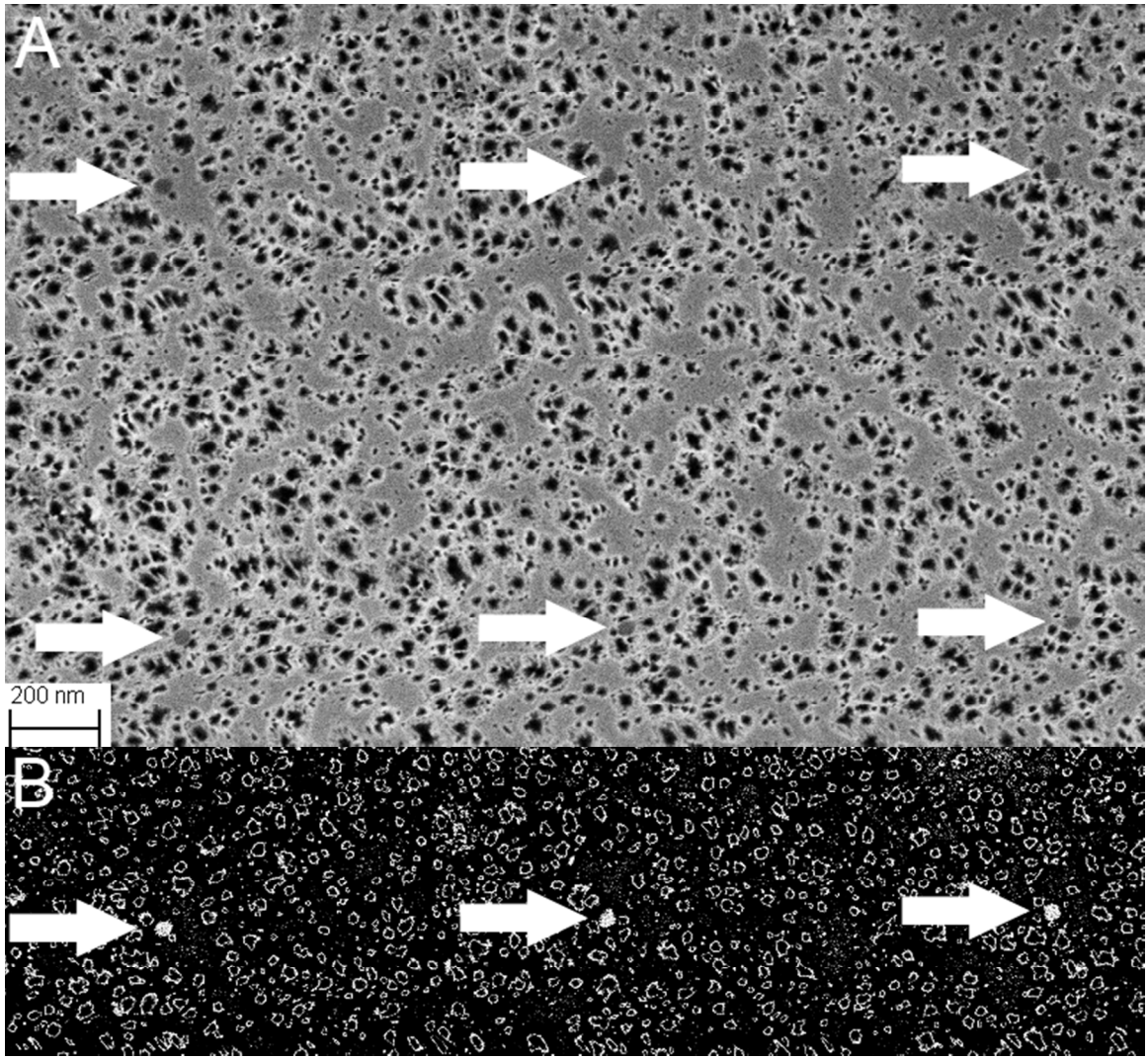

FIGURE S5: This SEM of planarized apertures shows the glass-filled apertures in the midst of planarized $Al_{95\%}Si_{4\%}Cu_{1\%}$ sputtered film. The 100 nm thick sputtered metal film conformally surrounded the glass pillars and provided a nearly pin-hole-free film. However, observing the apertures can be difficult amid the distinct metal grains. Observing the apertures is greatly aided by noticing the square lattice on which they are fabricated even with the slight SEM stage drift that occurs during image acquisition. (A) The original contrast from the SEM with six apertures indicated with white arrows. (B) A segment of the same image with a remapping of the grey scale curve to make the apertures appear white. In (B), the white arrows again point to the apertures but now the apertures are obvious as their relatively uniform shade of grey is highlighted.

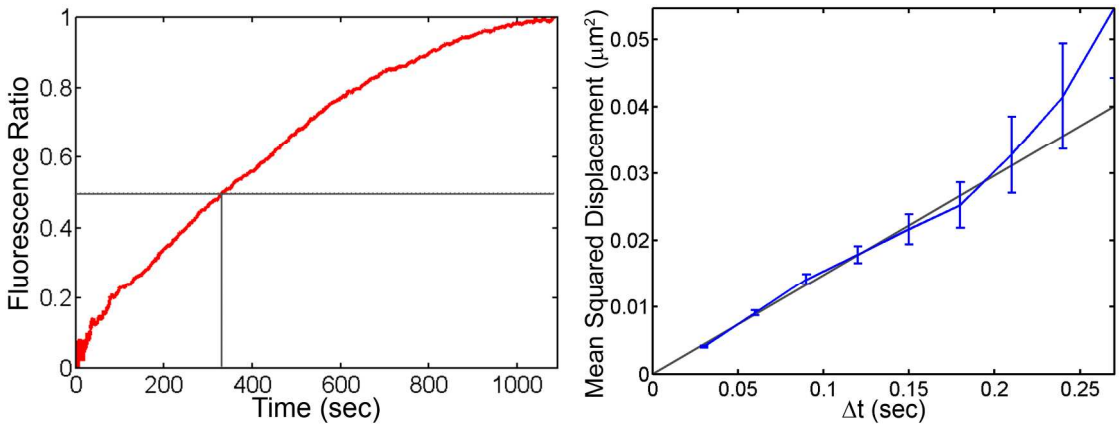

FIGURE S6: The diffusion coefficient (D) of CTxB in a POPC SLB was measured both by (A) fluorescence recovery after photobleaching (FRAP) and (B) single particle tracking (SPT) via stochastic optical reconstruction microscopy. The half time of recovery in FRAP was 330 s and D was calculated to be 0.11 ± 0.02 $\mu m^2/s$. The observed diffusion coefficient from SPT was 0.14 ± 0.01 $\mu m^2/s$, as demonstrated by the slope of the mean square displacement vs. Δt data.

SUPPLEMENTARY TABLE

Table S1: Indices of refraction used in FEA computations

	Incident Free-Space Wavelength (nm)			
Material	**215**	**279**	**365**	**488**
Air	1.00	1.00	1.00	1.00
Al	0.14-2.5i	0.24-3.3i	0.41-4.4i	0.73-5.9i
Au	-	-	-	1.05-1.8i
Cr	-	-	-	2.46-4.4i
SiO_2	1.53	1.49	1.47	1.46
photoresist	-	-	1.7-0.4i	-
H_20	-	1.37	-	1.34

SUPPLEMENTARY REFERENCES

(1) Xu, H. Z.; Zhu, P. S.; Craighead, H. G.; Webb, W. W. Resonantly Enhanced Transmission of Light through Subwavelength Apertures with Dielectric Filling. *Opt. Commun.* **2009**, *282*, 1467–1471.

(2) Jin, J.-M. *The Finite Element Method in Electromagnetics*; 2nd ed.; Wiley New York, 2002.

(3) Axelrod, D.; Koppel, D. E.; Schlessinger, J.; Elson, E.; Webb, W. W. Mobility Measurement by Analysis of Fluorescence Photobleaching Recovery Kinetics. *Biophys. J.* **1976**, *16*, 1055–1069.

(4) Manley, S.; Gillette, J. M.; Patterson, G. H.; Shroff, H.; Hess, H. F.; Betzig, E.; Lippincott-Schwartz, J. High-Density Mapping of Single-Molecule Trajectories with Photoactivated Localization Microscopy. *Nat. Methods* **2008**, *5*, 155–157.

(5) Shelby, S. A.; Holowka, D.; Baird, B.; Veatch, S. L. Distinct Stages of Stimulated FcεRI Receptor Clustering and Immobilization Are Identified through Superresolution Imaging. *Biophys. J.* **2013**, *105*, 2343–2354.

(6) York, A. G.; Ghitani, A.; Vaziri, A.; Davidson, M. W.; Shroff, H. Confined Activation and Subdiffractive Localization Enables Whole-Cell PALM with Genetically Expressed Probes. *Nat. Methods* **2011**, *8*, 327–333.

(7) Track.m, 1999; The Matlab Particle Tracking Code Repository: http://physics.georgetown.edu/matlab/code.html; (accessed Jul 7, 2014).